Heliyon 11 (2025) e42601

Contents lists available at ScienceDirect

Heliyon

journal homepage: www.cell.com/heliyon

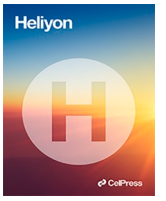

Research article

# The Cardiff Eye Shape Analysis Protocol (CESAP): Producing a digital representation of the anterior ocular surface

Jennifer M. Turner [a], Chi Hieu Le [b], Paul J. Murphy [c,*]

[a] Cardiff University, School of Optometry and Vision Sciences, Maindy Road, Cardiff, CF24 4HQ, UK
[b] University of Greenwich, School of Engineering, Central Avenue, Medway, ME4 4TB, UK
[c] University of Waterloo, School of Optometry and Vision Science, University Avenue West, Waterloo, N2L 3G1, Canada

ARTICLE INFO

*Keywords:*
Corneal topography
Ocular surface shape
Impression moulding
Laser scanning
Scleral lens

ABSTRACT

*Objective:* To develop a method for accurate 3-dimensional (3D) representation of the anterior ocular surface (AOS) based on ocular impression and reverse engineering of an AOS plaster biomodel.
*Methods:* An AOS plaster biomodel was fabricated using ocular impression and a developed casting support device (CSD) and landmark registration element (LRE) to stabilise and consistently fix the impression casting tray within the casting support during the casting process. The touch-trigger probe on a co-ordinate measurement machine (CMM) digitised the AOS plaster biomodel to represent the AOS shape. The CSD and LRE were manufactured using an Additive Manufacturing selective laser sintering (SLS) process. A single stainless-steel ball (diameter: 22 mm) was cast as a surrogate AOS biomodel using polyvinylsiloxane impression material. The surrogate biomodel which was used to evaluate material selection and stability of the AOS biomodels fabricated using the CSD and LRE, and to evaluate repeatability and reproducibility of the point cloud data collection methods. The points of circular profiles were measured at different Z values in mm: $z = -1$ mm, $z = -2$ mm, $z = -3$ mm, $z = -4$ mm and $z = -5$ mm.
*Results:* The measurements were highly repeatable with an acceptable tolerance. For the typical case of the surrogate AOS biomodel, the average distance of the digitised points to the best-fit sphere of all the digitised points from four measurements ranges from 0.002 to 0.010 mm. The shrinkage study of the surrogate AOS biomodels was conducted, with measurements taken one month apart for comparison. The analysis results showed that most of the surrogate AOS biomodels reduced in size but within an acceptable tolerance, in which the mean error is from 0.005 to 0.010 mm for the 2D circular profiles measured at $Z = -4$ mm.
*Conclusions:* The Cardiff Eye Shape Analysis Protocol (CESAP) provides a repeatable and consistent method for producing solid, white-plaster, representations of a plaster cast AOS biomodel. Casting an impression in white plaster (Novadur™) produces a consistent surrogate AOS biomodel of a single stainless-steel 22 mm diameter ball. CESAP can be used as a framework for consistently converting an ocular impression into a 'real' AOS model that can be reverse-engineered to create 3D CAD models of the AOS shape for potential applications in optical image (topographer) calibration, prosthetic shell and scleral lens design, and AOS database development.

* Corresponding author. University of Waterloo School of Optometry and Vision Science, 200 University Avenue West, Waterloo, N2L 3G1, Ontario, Canada.
*E-mail address:* pjmurphy@uwaterloo.ca (P.J. Murphy).

https://doi.org/10.1016/j.heliyon.2025.e42601
Received 17 July 2024; Received in revised form 31 January 2025; Accepted 10 February 2025
Available online 10 February 2025
2405-8440/© 2025 The Authors. Published by Elsevier Ltd. This is an open access article under the CC BY-NC-ND license (http://creativecommons.org/licenses/by-nc-nd/4.0/).

## 1. Introduction

Knowledge of anterior ocular surface (AOS) topography is important for contact lens fitting, ocular disease diagnosis, and ocular surgery planning. In particular, the shape and smoothness of the corneal surface forms a key component in the ocular optical system to produce a clear image on the retina. The measurement of AOS topography can be performed using optical reflectometry methods to produce a virtual topographical map [1], but an actual plaster cast model can also be produced using the impression moulding method [2]. Ocular impressions are used in the manufacture of custom scleral contact lenses and ocular prostheses [2–4]. An impression is taken of the eye using a plastic material that can be manipulated to mould to the shape of the eye, before rapidly setting as a negative image of the ocular surface shape [5]. From this mould, a positive plaster-cast is taken, which is used to guide scleral lens manufacture [6].

With the increasing use of scleral lenses for treating ocular surface disease, there is a renewed interest in understanding how the AOS changes across the limbal transition zone between the cornea and the sclera [6–10], Although wide-field optical topographers that can image the limbal zone are available [7,11–13], an actual representation of the AOS is of value in determining the reliability of these corneal topographers by comparing the virtual topographical map with the actual model determined using impression moulding. This has led to a return of interest in impression moulding [4].

Anatomical registration is an important requirement of the impression-making process since it is critical that both the mould and cast model are 'registered' correctly with the ocular anatomy. The clinical impression method described by Pullum (and summarised above) is sufficient for general clinical purposes [2], but it lacks reliability when undertaking ocular impression where the accurate measurement of anatomical features, registered according to the three cardinal meridians (x, y, z), is required, such as when assessing AOS topographer accuracy [10]. To our knowledge, there is no published report on a method to optimise anatomical registration when using ocular impression moulding.

This study therefore had two objectives: to develop a reliable method for anatomical registration of the AOS with the impression mould and the resultant plaster cast; and to assess whether the developed registration method was reliable in producing a precise and

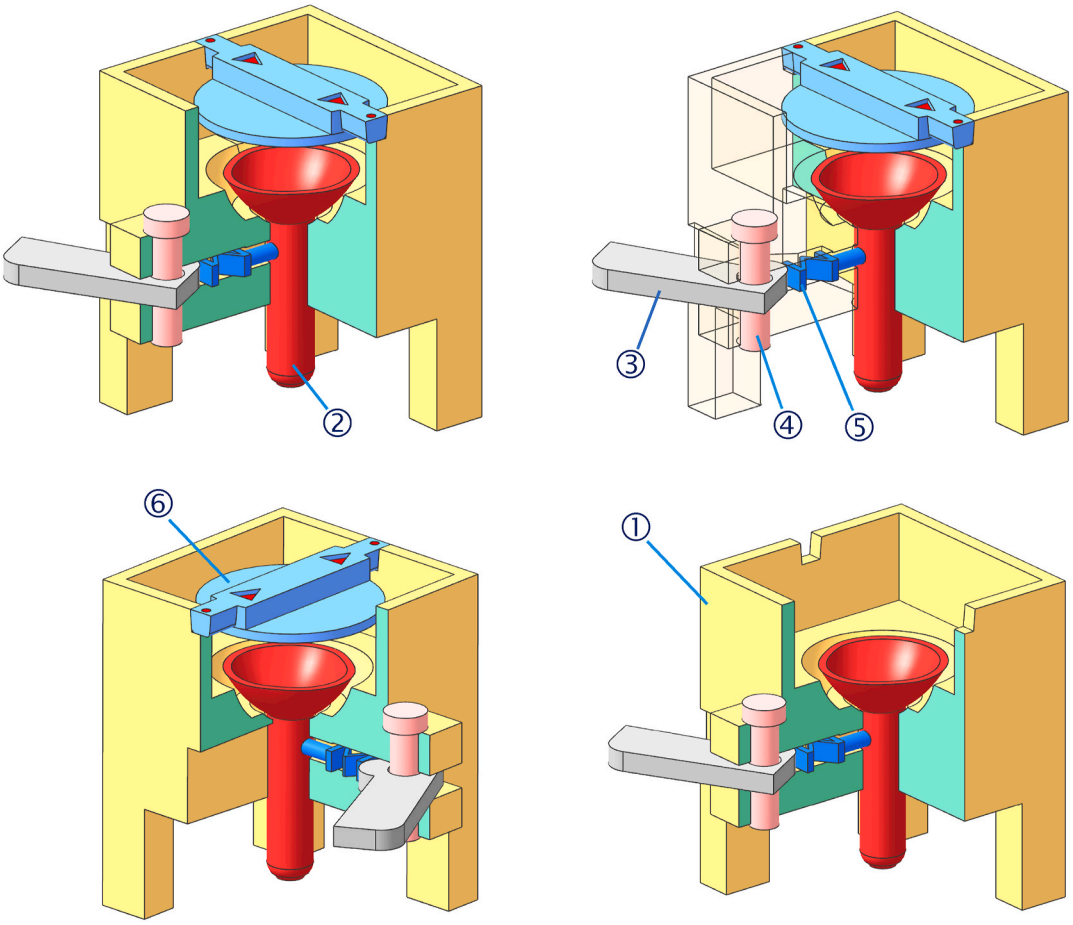


**Fig. 1.** 3D CAD assembly models with section views of a casting support device in assembly with a landmark registration element (LRE) including the following: A main frame (1), an impression casting tray (2), a locking mechanism (3–5) in which a spring (5) is introduced to fix an impression casting tray (2) to a main frame (1), and a landmark registration element (6) which is aligned with an impression tray (2) and a main frame (1).

repeatable biomodel of the AOS shape (repeatability and reproducibility (R&R) study).

## 2. Methods

### 2.1. Casting support and landmark registration element design

In order to reconstruct a three-dimensional (3D) model of the eye shape from the ocular impression casting trays (Cantor and Nissel Ltd, Brackley, UK), a casting support device and a registration element were designed and manufactured. Fig. 1 presents the 3D CAD (Computer Aided Design) assembly models of a casting support device and a registration element. The important design objective is that the impression casting tray needs to be stably and consistently fixed to the casting support during the casting process of fabricating the AOS plaster cast biomodel of the eye shape. In addition, to support a systematic investigation of a big number of 3D eye shapes, the ocular impression casting trays need to be correctly aligned with the relevantly used datum for processing 3D scanned point cloud data. With the design shown in Fig. 1, a locking mechanism with a spring element was introduced to fix an impression casting tray to the main frame of a device.

To maintain the correct alignment of the impression casting tray within the vertical eye meridian, a landmark registration element (LRE) was designed, as shown in Fig. 2 (A). In Fig. 1, the LRE can be assembled to the main frame of a device with the relevant direction and alignment based on the triangle landmarks. The LRE is then used as the base of the AOS plaster cast or biomodel of the eye shape as shown in Fig. 3 (B, C, D). This method means that the LRE became an integral part of the AOS plaster cast once the plaster had set and adhered to the polyamide material of the LRE. The LRE is aligned with the vertical meridian of the impression casting tray and was held in position during the cast drying period by two notches in the casting support device (Fig. 1).

In this way, the datum of the ocular impression casting tray is "systematically" determined; and is consistent from the eye impression process to the scanned 3D data set (Fig. 2). This is important because the less involvement of manual methods and the more consistence in the way in which the data is collected, the better the solution in the further analysis steps that will be obtained. It is

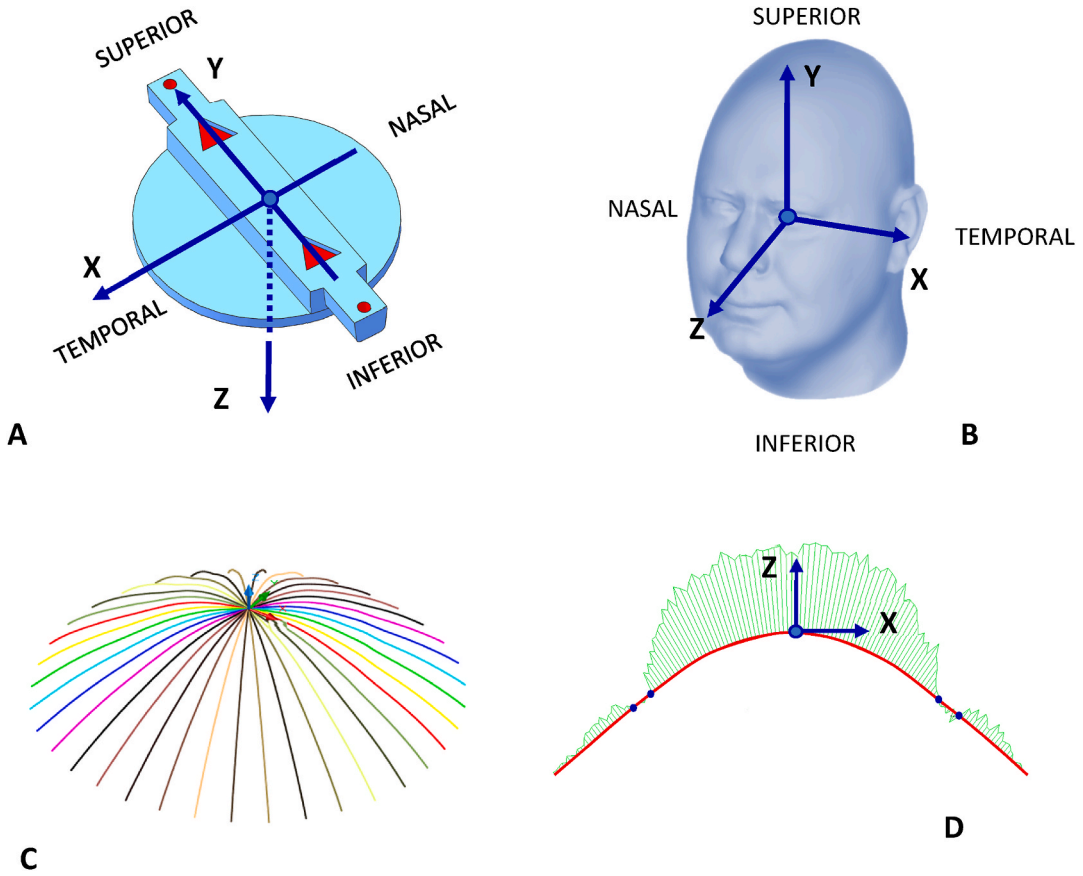


**Fig. 2.** Design of a landmark registration element (LRE) showing alignment with the cardinal directions of the eye (x, y, z). A: The LRE with the introduced triangle marks to show the vertically aligned ridge on the LRE inferior surface. B: The coordinate systems XYZ for the eye are used for registration and processing of the scanned data points. C: The AOS profiles created from the scanned point cloud data of the AOS plaster cast or biomodel of the eye shape. D: The AOS cross-profile in the XZ plane. The red curve is the AOS cross-profile in the XZ plane, and the curvature at different positions of the AOS cross-profile is shown in green.

noted that, the base of the LRE was designed to include a ridge that could be clamped into the fixture or jig for the Reverse Engineering (RE) process, in which high-precision laser scanners and co-ordinate measurement machines (CMMs) can be used to collect point cloud data that represent the geometry of the AOS shape. The casting support device and the LRE were manufactured using Additive Manufacturing (AM) or 3D Printing, the selective laser sintering (SLS) process (Fig. 3).

An ocular impression casting tray was scanned using a touch-trigger probe installed on a Mitutoyo CMM machine - CRA Apex C Model (2005) (Mitutoyo (UK) Ltd, Andover, UK). The digitised surface data of the impression tray was then exported to the RE software package (Geomagic, 3D Systems Inc, South Carolina, USA) and a non-uniform rational B-spline (NURBS) CAD model of the AOS shape was reconstructed, with the 3D cross profiles shown in Fig. 2(C and D).

The produced 3D printed casting support device with an impression casting tray in place is presented in Fig. 3 (A), in which the locking device is on the upper right side, and the AOS plaster cast or biomodel of the AOS shape which were successfully fabricated with the Type IV dental stone material (ULTIMA Novadur™), using the casting support device and the LRE in shown in Fig. 3 (B). As mentioned, the base of the LRE included a ridge that could be clamped into the fixture or jig for the RE process (Fig. 3(C and D)), in which high-precision laser scanners and CMMs were used to collect point cloud data that represents the geometry of the AOS shape. Both non-contact and contact techniques of RE were used for data collection to reconstruct 3D models of the AOS shape from the AOS plaster casts.

### 2.2. *Prototyping and testing of a surrogate AOS biomodel*

The accuracy of reproducibility and the stability of the AOS biomodels are important for reconstruction of 3D CAD models of the AOS shape. In addition, the selection of relevant data collection methods, including the contact method using the CMMs with the touch-trigger probes and the non-contact method using the high-precision laser scanners, depends very much on the property of a material used for fabricating AOS biomodels. The shrinkage issues also need to be taken into account. Therefore, it is necessary to investigate the repeatability and reproducibility of the data collection methods, and to develop an optimal solution for data collection and processing to mimimise possible errors and inconsistency when working on the point data processing to reconstruct 3D CAD models of the AOS shape. A single stainless-steel ball with a diameter of 22 mm was cast as a surrogate AOS biomodel using the polyvinylsiloxane impression material Tresident™ (Shütz Dental Group GmbH, Germany), which was used for (1) evaluations of

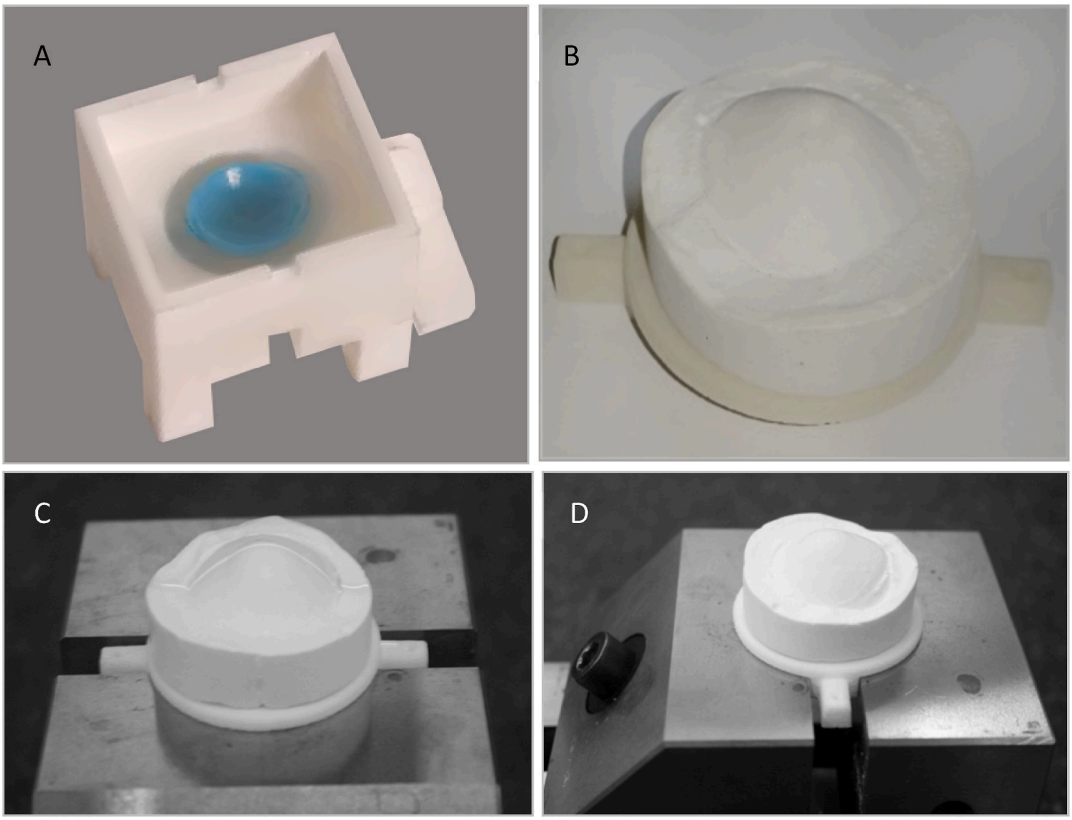


**Fig. 3.** A: The 3D printed casting support device with an impression casting tray in place in which the locking device is on the upper right side. B: The AOS plaster cast or biomodel of the AOS shape, in which the LRE is an integral part of the AOS plaster cast once the plaster had set and adhered to the polyamide material of the LRE. C & D: The base of the LRE was designed to include a ridge that could be clamped into the fixture or jig for the RE process, in which high-precision laser scanners and CMMs can be used to collect point cloud data that represent the geometry of the AOS shape.

material selection and stability of the AOS biomodels which are fabricated using the casting support device and LRE, and (2) evaluation of repeatability and reproducibility of the data collection methods, using the contact and non-contact methods (CMMs and high-precision laser scanners). A previous study by our group found that Tresident™ was quicker, more effective, and produced less ocular surface staining than an alternative irreversible hydrocolloid material [5]. Tresident™ also has minimal impression shrinkage (0.2%–1% shrinkage after 24 h) and is unaffected by humidity [5].

Tresident™ was dispensed into an impression shell and the shell/material combination pressed against the stainless-steel ball. Extra-hard, white plaster, Novadur™ (Ultima, Seiches-sur-Loir, France), a Type 4 Gypsum plaster, which conforms to ISO 6873:2013 (International Organisation for Standards) [14], was identified as a suitable compound to be used in conjunction with Tresident™. This product has excellent adhesion to the polyamide powder used in the SLS manufacturing process which is used to fabricate the LRE. Importantly, the published expansion of Novadur™ is only 0.15 % after 2 h [5]. A series of 12 AOS biomodels (such as those shown in Fig. 3 (B, C, D)) was manufactured using the same methods of fabricating a surrogate AOS biomodel of the 22 mm stainless-steel ball, using the casting support device and LRE (Fig. 1).

The surrogate AOS biomodel of the 22 mm stainless-steel ball was scanned using a touch-trigger probe installed on a CMM Mitutoyo CMM machine - CRA Apex C Model (2005) (Mitutoyo (UK) Ltd, Andover, UK) to ensure a high accuracy of data collection and measurements (±0.001 mm) [15].

### 2.3. Data acquisition and analysis of repeatability, reproducibility and stability of the AOS biomodels

Non-contact methods, such as laser scanning, were not used in the repeatability and reproducibility (R&R) study and the investigation of stability of the AOS biomodels due to: (1) their low accuracy (±20–25 μm) in comparison with a contact method using a touch-trigger or contact probe (1–5 μm); (2) the complexity in data processing of non-contact methods; and (3) the data collection and processing of the contact method using Renishaw touch-trigger probes (Renishaw plc, Wotton-under-Edge, UK) installed in the CMM can be implemented automatically through CMM programs and data processing algorithms.

Fig. 4 presents the data collection plan with the coordinate system or datum set-up for data collection using the CMM with the touch-trigger probes. The points of circular profiles are measured at different Z value: z = −1 mm, z = −2 mm, z = - 3 mm, z = −4 mm and z = −5 mm. The CMM can be programmed to automatically measure the coordinates of points with respect to the established datum or part coordinate system. The distance between two points in each circular profile is about 0.5 mm. The Renishaw touch-trigger probe was used for data collection. The trigger force of touch probes can be adjusted, and the smallest trigger force was used to minimise the influence of contact forces on measurements. For Renishaw's touch-trigger probes, the trigger force range varies from 0.07 N to 0.5 N, depending on the stylus length and probe type [16].

With this data collection plan, to assess repeatability and reproducibility (R&R study) of the data collection method, 3 surrogate AOS biomodels of the 22 mm diameter stainless-steel ball were used. There were, in total, 12 measurements (4 measurements for each surrogate AOS biomodel of the stainless-steel ball) completed at different times and by different machine operators, using the same measurement program to operate the CMM (Mitutoyo CMM machine - CRA Apex C Model (2005), (Mitutoyo (UK) Ltd, Andover, UK). Each machine operator operated the CMM 4 times to measure the points that present the circular profiles. For each measurement, the points that present the circular profiles at different Z values (z = −1 mm, z = −2 mm, z = - 3 mm, z = −4 mm and z = −5 mm) were measured and the coordinates of these points were automatically generated in *.asc file format. For better data management, the point data files and the AOS biomodels were coded as follow: (1) **Bb22**1, **Bb22**2 and **Bb22**3 indicates which surrogate AOS biomodel of the 22 mm diameter stainless-steel **b**all number 1, 2 and 3 respectively; and (2) the point date files **Bb22**1_M1.asc and **Bb22**1_M2.asc are created from the measurements M1 and M2, respectively, for the surrogate AOS biomodel of the 22 mm diameter stainless-steel **b**all number 1. The relevant codes are used for the point data files to assist in data acquisition and processing, especially when using

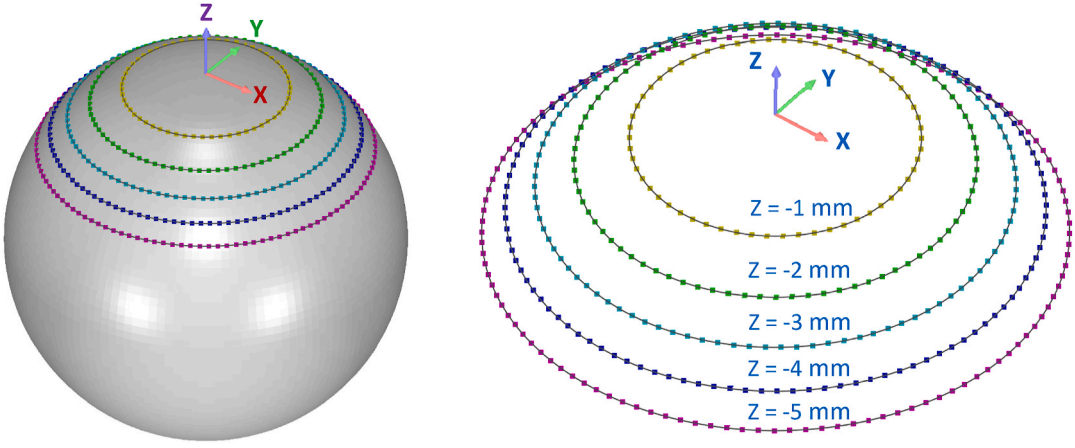


**Fig. 4.** The datum set-up and the plan for data collection using the CMM with the touch-trigger probes, in which the points of circular profiles are measured at different Z values: z = −1 mm, z = −2 mm, z = - 3 mm, z = −4 mm and z = −5 mm.

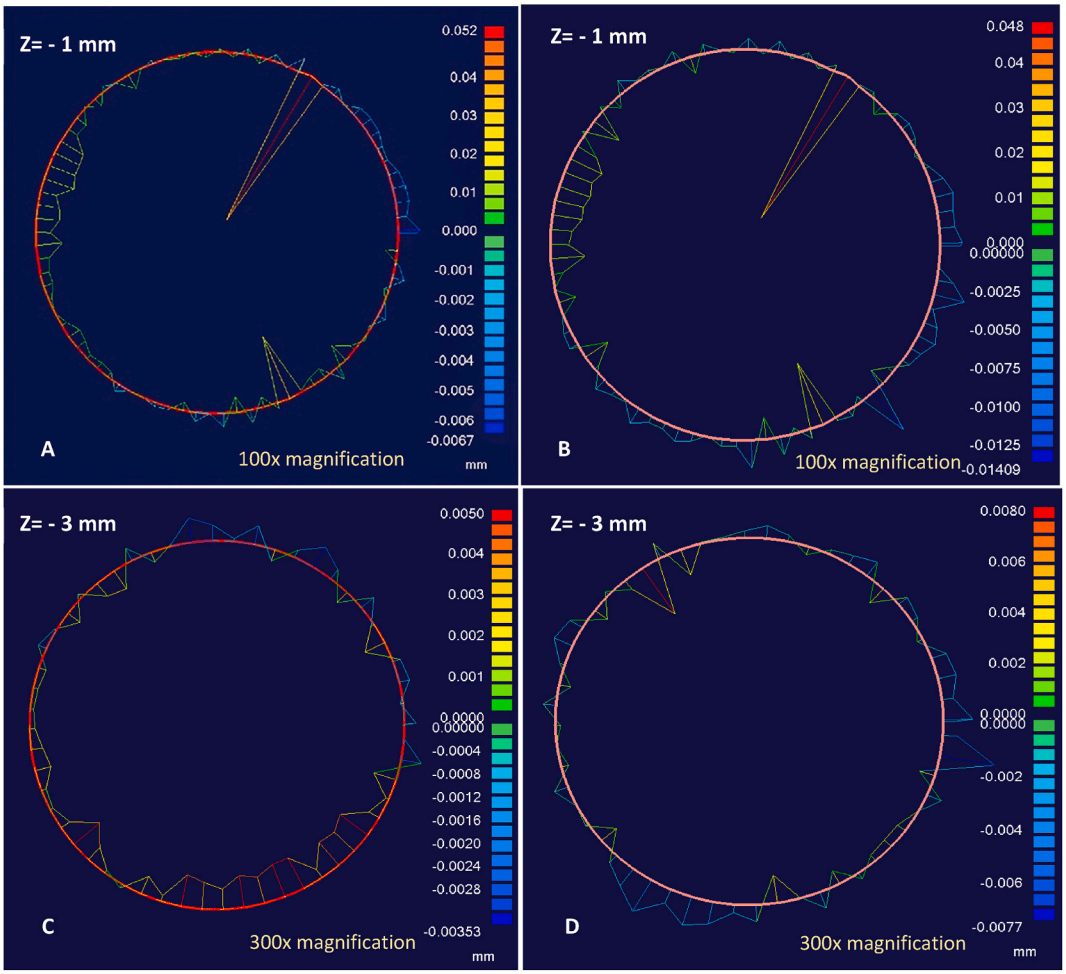


**Fig. 5.** Example of the LSC radial plots showing comparisons of the measured 2D circular profiles of the surrogate AOS biomodel **Bb221**. **A**: A comparison between the first and the second measurement in which a 2D circular profiles were measured at $z = -1$ mm. **B**: A comparison between the first and the third measurement in which a 2D circular profiles were measured at $z = -1$ mm. **C**: A comparison between the first and the second measurement in which a 2D circular profiles were measured at $z = -3$ mm. **D**: A comparison between the first and the third measurement in which a 2D circular profiles were measured at $z = -3$ mm. It is noted that, due to the size limitation of the figure, the error map cannot be seen because of the small value of dimensional errors. A magnification of 100x and 300x was used to highlight the error maps in millimetres.

programming solutions to automate the steps of processing point data.

A laser scanning system, HYSCAN 45c (Hymarc Ltd, Ottawa, Canada), was also used for non-contact data acquisition from the AOS biomodels of the 22 mm diameter stainless-steel ball, as well as the AOS biomodels of the eye shape as shown in Fig. 3 (B, C, D). With the use of laser scanning, there is no physical contact with the AOS biomodels, and the data collection is very fast. The calibration accuracy of the laser scanning system is from ±0.020 mm to ±0.025 mm. While the laser scanning is known to be less accurate than point-to-point sensing with touch-trigger probes, early testing using the model prototypes suggested that the combined system error of the laser scanning and data processing was ±0.065 mm (maximum), which is comparable to the repeatability of modern ocular surface imaging methods and is close to the manufacturing tolerance for gas permeable corneal contact lenses (±0.05 mm, back optic zone radius, (ISO 18369–2:2017; International Organisation for Standards) and scleral contact lenses (±0.1 mm, back optic zone radius (ISO 18369–2:2017; (International Organisation for Standards) [17].

## 3. Results

Measurements for each circle of sagittal depth were presented as radial plots or deviation maps using the least squares circles (LSC) method [18]. This method produced a circle that shows the difference in the sum of the squares of the deviation for the expected circle and the measurement data. Fig. 5 presents an example of the LSC radial plot showing a comparison between the first and second measurements of the surrogate AOS biomodel **Bb22**1 (the 22 mm diameter stainless-steel ball number 1), measured at z = −1 mm and z = - 3 mm, in which the plots were colour-coded to provide a visualisation of positive error as hot colours (light green to red) and negative error as cold colours (dark green to dark blue).

For a better understanding and investigation of repeatability, reproducibility and stability of the AOS biomodels, the deviation or error maps between the digitised points of the AOS biomodel of the 22 mm diameter stainless-steel ball and the best fit sphere of all the digitalised points from 4 measurements were created (Fig. 6).

Table 1 presents the summary about the deviation or error maps shown in Fig. 6, for the 4 measurements of the AOS biomodel

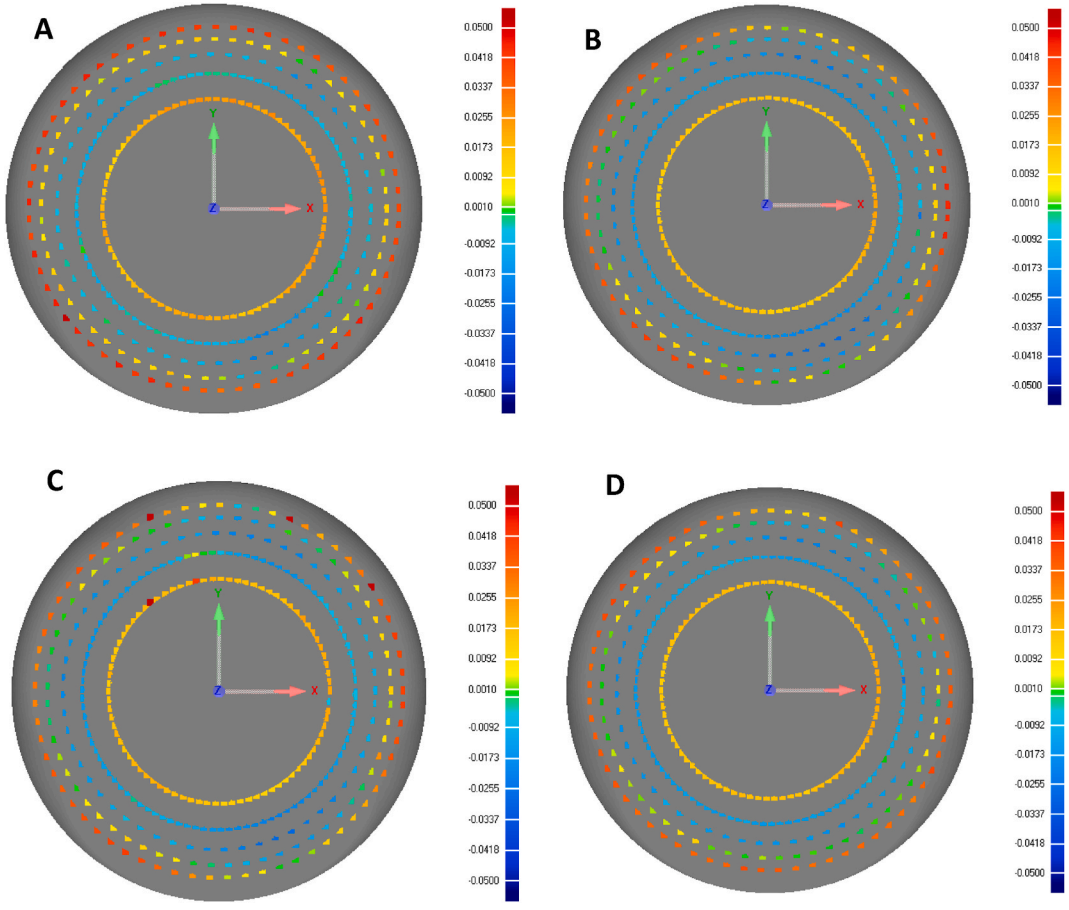


**Fig. 6.** The deviation or error maps between the digitised points of the AOS biomodel **Bb22**1 of the 22 mm diameter stainless-steel ball and the best fit sphere of all the digitalised points from 4 measurements. **A**: The error map for the first measurement (**Bb22**1_M1). **B**: The error map for the second measurement (**Bb22**1_M2). **C**: The error map for the third measurement (**Bb22**1_M3). **D**: The error map for the fourth measurement (**Bb22**1_M4).

**Table 1**
The deviation analysis between the digitised points of the AOS biomodel **Bb221** of the 22 mm diameter stainless-steel ball and the best fit sphere of all the digitalised points from 4 measurements. RMS stands for Root Mean Square.

| | Bb221_M1 | Bb221_M2 | Bb221_M3 | Bb221_M4 |
|---|---|---|---|---|
| Positive Maximum Distance | 0.0501 | 0.0456 | 0.1048 | 0.0406 |
| Negative Maximum Distance | −0.0233 | −0.0279 | −0.0288 | −0.0249 |
| Average Distance | 0.0096 | 0.0022 | 0.0031 | 0.0038 |
| Positive | 0.0237 | 0.0187 | 0.0199 | 0.0190 |
| Negative | −0.0090 | −0.0138 | −0.0135 | −0.0137 |
| Standard Deviation | 0.0194 | 0.0186 | 0.0197 | 0.0187 |
| RMS Estimate | 0.0216 | 0.0187 | 0.0200 | 0.0191 |

**Table 2**
The deviation analysis between the digitised points of the AOS biomodels **Bb221**, **Bb222** and **Bb223** of the 22 mm diameter stainless-steel ball and the best fit sphere of all the digitalised points from 12 measurements. RMS stands for Root Mean Square.

| | Bb221_1b | Bb221_2b | Bb221_3b | Bb221_4b | Bb222_1b | Bb222_2b |
|---|---|---|---|---|---|---|
| Positive Maximum Distance | 0.0274 | 0.0237 | 0.0791 | 0.0190 | 0.0522 | 0.0492 |
| Negative Maximum Distance | −0.0338 | −0.0410 | −0.0405 | −0.0371 | −0.0813 | −0.0521 |
| Average Distance | −0.0034 | −0.0170 | −0.0099 | −0.0092 | −0.0083 | −0.0017 |
| Positive | 0.0167 | −0.0170 | 0.0134 | 0.0123 | 0.0167 | 0.0195 |
| Negative | −0.0174 | 0.0121 | −0.0227 | −0.0224 | −0.0242 | −0.0155 |
| Standard Deviation | 0.0177 | 0.0181 | 0.0191 | 0.0177 | 0.0250 | 0.0194 |
| RMS Estimate | 0.0180 | 0.0210 | 0.0215 | 0.0200 | 0.0264 | 0.0195 |
| | Bb222_3b | Bb222_4b | Bb223_1b | Bb223_2b | Bb223_3b | Bb223_4b |
| Positive Maximum Distance | 0.0412 | 0.0461 | 0.1035 | 0.0115 | 0.0147 | 0.0115 |
| Negative Maximum Distance | −0.0414 | −0.0410 | −0.1144 | −0.1068 | −0.0063 | −0.0104 |
| Average Distance | −0.0015 | −0.0020 | 0.0236 | 0.0292 | 0.0290 | 0.0320 |
| Positive | 0.0169 | 0.0176 | 0.0358 | 0.0377 | 0.0386 | 0.0392 |
| Negative | −0.0144 | −0.0154 | −0.0173 | −0.0192 | −0.0184 | −0.0220 |
| Standard Deviation | 0.0172 | 0.0177 | 0.0326 | 0.0320 | 0.0331 | 0.0317 |
| RMS Estimate | 0.0173 | 0.0178 | 0.0402 | 0.0433 | 0.0440 | 0.0451 |

**Bb221** of the 22 mm diameter stainless-steel ball, respectively **Bb221**_M1, **Bb221**_M2, **Bb221**_M3 and **Bb221**_M4.

Similarly, the error maps for comparison of the digitised points of the AOS biomodels **Bb221**, **Bb222** and **Bb223** and the best fit sphere of all the digitalised points from 12 measurements were created (Appendix 1), and the summary about the deviation or error maps is presented in Table 2. The data from Tables 1 and 2 show that, the repeatability and reproducibility of the data collection methods are acceptable.

The shrinkage study of the AOS biomodels was conducted with measurements taken one month apart for comparison. The analysis results showed that most of the surrogate AOS biomodels reduced in size but within an acceptable tolerance, in which the mean error is from 0.005 to 0.010 mm for the 2D circular profiles measured at Z = −4 mm.

## 4. Discussion and conclusions

This paper describes the investigation of a method of transferring the anatomical registration from an ocular impression to a plaster cast representation, and reports on the validation of the method, which we have called the Cardiff Eye Shape Analysis Protocol (CESAP). It provides evidence to support the use of the protocol for wide field topographic data collection using ocular impression from the human AOS *in-vivo*, to a standard acceptable to industry and clinical requirements.

Detailed knowledge of AOS topography is essential for ophthalmic clinical practice that involves eye shape. Measurement based on optical methods has been the most common approach due to their speed of measurement and analysis. However, optical methods are limited, with some exceptions [1,7], to the corneal region, due to a deterioration in the sharpness of the optical reflections in limbal area and across the conjunctiva. The increasing use of scleral lenses for optical correction and ocular surface disease management has increased the interest in AOS shape beyond the cornea [8,9]. AOS impression-taking using a mouldable material has been a long-standing method for large scale AOS representation and has been used in the manufacture of prosthetic eye shells and scleral contact lenses. However, detailed analysis of the change in AOS shape at the small scale, using laser scanning, has not been made until recently [4]. A significant challenge for accurate measurement has been a consistent method for producing the solid, 'real', plaster model of the AOS. Plaster casting, by itself is very simple, but a consistent approach for registration of the orientation of the AOS is more challenging. The results from this paper demonstrate that the Cardiff Eye Shape Analysis Protocol (CESAP) provides a repeatable and consistent method for producing solid, white plaster representations of the AOS biomodels.

This investigation has provided evidence to validate the combined use of ocular impression taking and the CESAP to provide a reliable system for collecting topographic data for a surrogate AOS biomodels of the 22 mm diameter stainless-steel ball. The casting support device and landmark registration elements, when combined, can provide a consistent orientation registration system.

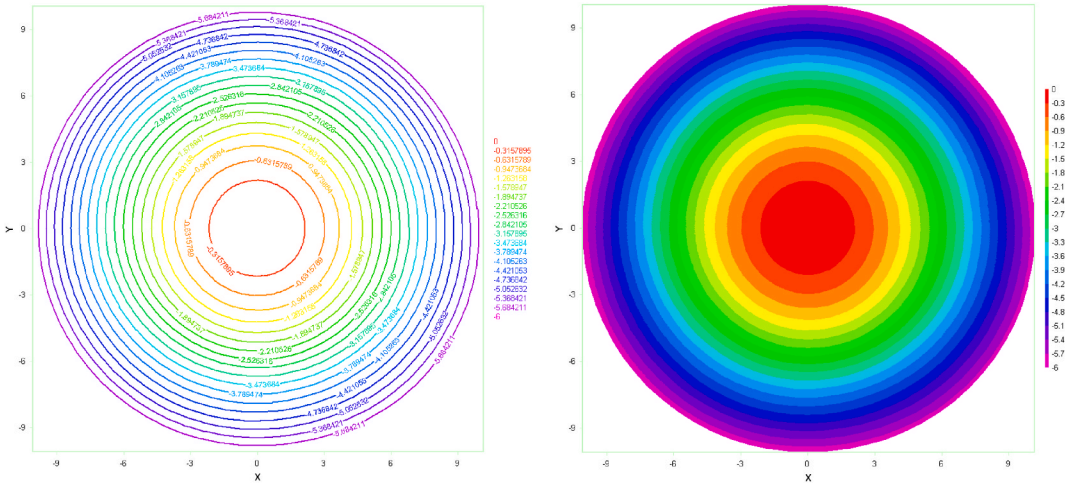

**Fig. 7.** The height contour maps of the mean geometry of the AOS shape calculated from 120 AOS biomodels of the right eyes of the European population.

Individual casts made from a series of impressions (using Tresident™ material and cast using Novodur™ plaster) were consistent in repeatability, reproducibility, and stability of material. The measurements were highly repeatable with an acceptable tolerance; for the case of **Bb22**1, the average distance of the digitised points to the best fit sphere of all the digitalised points from 4 measurements is from 0.002 to 0.010 mm.

This protocol for obtaining consistent 'real' AOS shape has several applications. Firstly, surface impression-taking, combined with plaster casting and reverse engineering, allows the comparison of a 'virtual' optical method with the 'real' surface shape. This permits the testing of instrument accuracy and provides a method for improving calibration.

Secondly, by having an accurate digital representation of the ocular surface, the design and manufacture of prosthetic shells and custom scleral lenses can be improved [19]. Scleral lens manufacture using ocular impression-taking is long-established. CESAP provides a high level of accuracy which is important in the manufacture of custom designs for highly irregular AOS shapes.

Thirdly, CESAP enables a consistent approach, including landmark registration, that is essential when gathering ocular impressions to incorporate into a 'real' AOS database. In another study not reported here, CESAP was successfully applied to create a database of 3D models of real AOS shapes. Fig. 7 presents the height contour maps of the mean geometry of the AOS shape, calculated from 120 AOS biomodels of the right eyes of a European population. This database can be used to better understand normative population topographical variation associated with ethnicity or refractive error or can be used to describe the variation of support the design and development of new types of contact lenses.

CESAP provides a framework for consistently converting an ocular impression into a 'real' AOS model that can be reverse engineered to create 3D CAD models of the AOS shape. These 3D CAD models have potential applications in optical image (topographer) calibration, prosthetic shell and scleral lens design, and AOS database development [20].

## CRediT authorship contribution statement

**Jennifer M. Turner:** Writing – original draft, Project administration, Investigation, Formal analysis, Data curation, Conceptualization. **Chi Hieu Le:** Writing – review & editing, Validation, Software, Resources, Methodology, Investigation, Formal analysis, Conceptualization. **Paul J. Murphy:** Writing – review & editing, Validation, Supervision, Resources, Project administration, Methodology, Funding acquisition, Conceptualization.

## Funding

This study was supported by a collaborative partnership between Cardiff University and Menicon (Japan) Ltd. The authors have no proprietary or commercial interests in any of the materials discussed in this article.

## Declaration of competing interest

The authors declare the following financial interests/personal relationships which may be considered as potential competing interests:Jennifer Turner reports financial support was provided by Menicon Co Ltd. If there are other authors, they declare that they have no known competing financial interests or personal relationships that could have appeared to influence the work reported in this paper.

**Appendix 1. The deviation or error maps between the digitised points of the AOS biomodels Bb221, Bb222, Bb223 and Bb224 of the 22 mm diameter stainless-steel ball and the best fit sphere of all the digitalised points from 4 measurements**

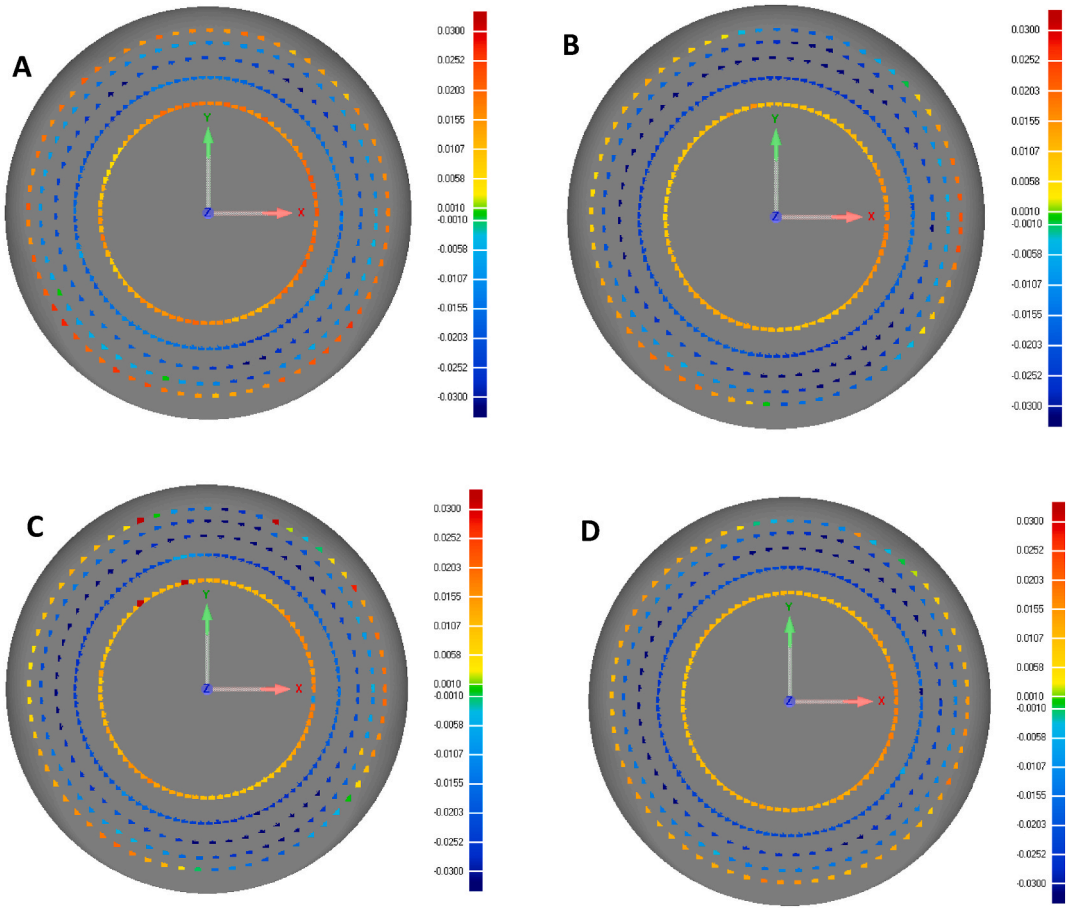


**Fig. A1.** The deviation or error maps between the digitised points of the AOS biomodel **Bb22**1 of the 22 mm diameter stainless-steel ball and the best fit sphere of all the digitalised points from 4 measurements. **A**: The error map for the first measurement (**Bb22**1_M1). **B**: The error map for the second measurement (**Bb22**1_M2). **C**: The error map for the third measurement (**Bb22**1_M3). **D**: The error map for the fourth measurement (**Bb22**1_M4).

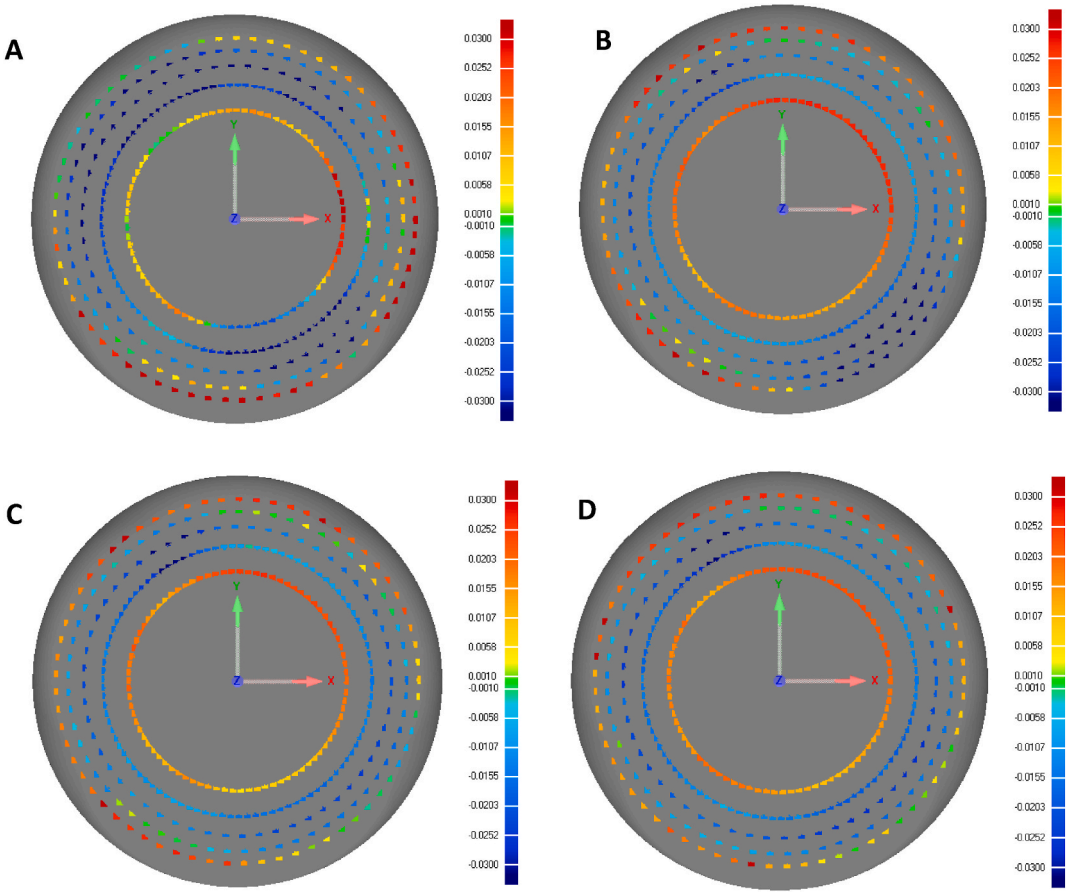


**Fig. A2.** The deviation or error maps between the digitised points of the AOS biomodel **Bb222** of the 22 mm diameter stainless-steel ball and the best fit sphere of all the digitalised points from 4 measurements. **A**: The error map for the first measurement (**Bb222**_M1). **B**: The error map for the second measurement (**Bb222**_M2). **C**: The error map for the third measurement (**Bb222**_M3). **D**: The error map for the fourth measurement (**Bb222**_M4).

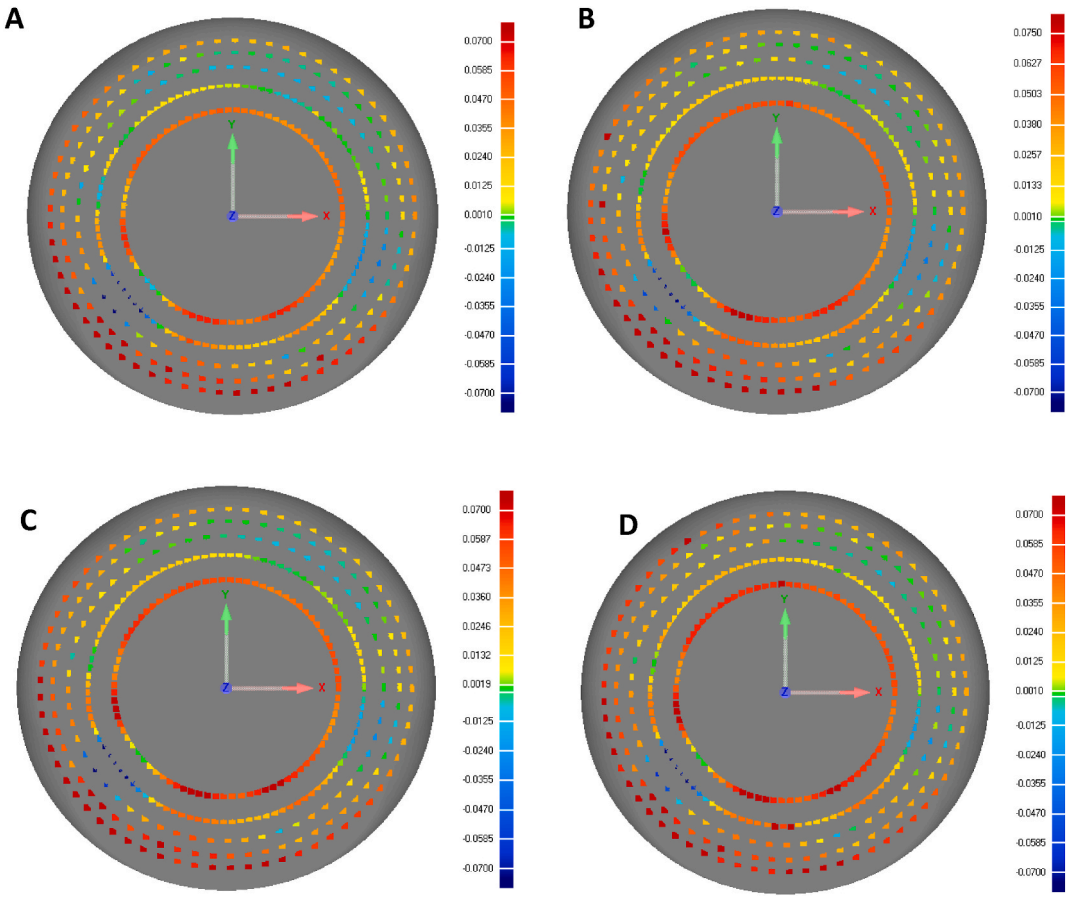


**Fig. A3.** The deviation or error maps between the digitised points of the AOS biomodel **Bb22**3 of the 22 mm diameter stainless-steel ball and the best fit sphere of all the digitalised points from 4 measurements. **A:** The error map for the first measurement (**Bb22**3_M1). **B**: The error map for the second measurement (**Bb22**3_M2). **C**: The error map for the third measurement (**Bb22**3_M3). **D**: The error map for the fourth measurement (**Bb22**3_M4).

## References


[1] D.R. Iskander, P. Wachel, P.N. Simpson, A. Consejo, D.A. Jesus, Principles of operation, accuracy and precision of an eye surface profiler, Ophthal Physiol Opt 36 (2016) 266–278.
[2] K.W. Pullum, Eye impressions, in: A.J. Phillips, L. Speedwell, J. Morris (Eds.), Contact Lenses, 5 ed., Elsevier Butterworth-Heineman, 2007, p. 343.
[3] M. Barnett, C. Courey, D. Faddi, K. Lee, L. Michaud, G. Montani, E. van der Worp, S.V. Vincent, M. Walker, P. Bilkhu, P. Morgan, Bcla clear – scleral lenses, Cont Lens Anterior Eye 44 (2021) 270–288.
[4] A. Nau, E.S. Shorter, J.S. Harthan, J.S. Fogt, C.B. Nau, M. Schornack, Multicentre review of impression-based scleral devices, Cont Lens Anterior Eye 44 (2021) 1–6.
[5] J.M. Turner, C. Purslow, P.J. Murphy, Ocular impression-taking – which material is best? Eye Contact Lens 45 (2019) 55–60.
[6] T.J. Bowden, Development of scleral contact lenses, in: Contact Lenses, the Story, Bower House Publications, Kent, 2009, pp. 76–86.
[7] G. DeNaeyer, D. Sanders, E. van der Worp, J. Jedlicka, L. Michaud, S. Morrison, Qualitative assessment of scleral shape patterns using a new wide field ocular surface topographer: the SSSG Study, J Contact Lens Res Sci 1 (2017) 12–22.
[8] M. Ritzmann, P.J. Caroline, R. Börret, E. Korszen, An analysis of anterior corneal shape and its role in the design and fitting of scleral contact lenses, Cont Lens Anterior Eye 41 (2018) 205–213.
[9] M. Muzyka-Woźniak, A. Oleszko, Ł. Stróżecki, S. Woźniak, The corneo-scleral junction assessed with optical coherence tomography, PLoS One 17 (2022) e0278884.
[10] K.A. Tuan, E. McDonald, C.W. Sindt, Population ocular topography analysis using impression-based elevation data, Investig. Ophthalmol. Vis. Sci. 63 (2022) 536. A0234.
[11] D.A. Jesus, R. Kedzia, D.R. Iskander, Precise measurement of scleral radius using anterior eye profilometry, Cont Lens Anterior Eye. 40 (2017) 47–52.
[12] L. Sclafani, D. Slater, B. Lay, C.W. Sindt, Topographic elevation data to design scleral lenses, Investig. Ophthalmol. Vis. Sci. 58 (2017) 3550.
[13] C.W. Sindt, B. Lay, R. Danno, Repeatability and validation of Scheimpflug scleral data, Investig. Ophthalmol. Vis. Sci. 59 (2018) 1774.
[14] ISO 6873:2013 Dentistry. Gypsum Products (Reviewed 2024). Geneva: International Organisation for Standards.
[15] D.T. Pham, Hieu Le Chi, Reverse engineering - hardware and software, in: V. Raja, K.J. Fernandes (Eds.), Reverse Engineering - an Industrial Perspective, Springer-Verlag, London, 2008, pp. 33–69.
[16] Renishaw, Trigger force gauge, Available at: https://www.renishaw.com, 2024. (Accessed 29 January 2025).
[17] ISO 18369-2, Ophthalmic Optics. Contact Lenses (Reviewed 2023), International Organisation for Standards, Geneva, 2017. Tolerances.

[18] W. Sui, D. Zhang, Four methods for roundness evaluation, Phys. Procedia 24 (2012) 2159–2164.
[19] J. Reinhard, P. Urban, S. Bell, D. Carpenter, M.S. Sagoo, Automatic data-driven design and 3D printing of custom ocular prostheses, Nat. Commun. 15 (2024) 1360.
[20] A. Consejo, C. Llorens-Quintana, H. Radhakrishnan, D.R. Iskander, Mean shape of the human limbus, J. Cataract Refract. Surg. 43 (2017) 667–672.